Intrinsic-Dipole-Regulated Carrier Lifetimes in Five-Atomic-Layer Janus Group-III Chalcogenides for Photovoltaic Applications

Yifan Wu（吴一凡）[1,2], Shi-Qi Li（李仕琪）[1,2*], Yuee Xie（谢月娥）[1,2*], Yuanping Chen（陈元平）[1,2*]

1. School of Physics and Electronic Engineering, Jiangsu University, Zhenjiang, Jiangsu 212013, China.
2. Quantum Sensing and Agricultural Intelligence Detection Engineering Center of Jiangsu Province, Zhenjiang 212013, China.
Corresponding authors: shiqili@ujs.edu.cn, yueex@ujs.edu.cn, chenyp@ujs.edu.cn.

Abstract

The intrinsic out-of-plane polarity of two-dimensional (2D) Janus materials provides a natural route to regulate photogenerated carrier dynamics. Here, we study electronic structures, stability, and carrier recombination dynamics of five-atomic-layer Janus group-III chalcogenide monolayers with chemical formulas MNS_3, $MNSSe_2$, and $MNSTe_2$, where M and N represent In, Ga, and Al. Strongly tunable carrier lifetimes have been found in these Janus monolayers. After structural stability screening, the carrier recombination time varies from 0.27 ns in $InGaSTe_2$ to 1272.8 ns in $InAlS_3$, showing a change over more than four orders of magnitude. Moreover, the maximum photocurrent of $InAlS_3$ reaches 4.13 a_0^2/photon, highlighting its potential for high-efficiency photovoltaic applications. By calculating band-edge charge densities, electrostatic potentials, nonadiabatic couplings, and pure-dephasing times, we find that the lifetime variation is closely related to the built-in electric field and band-edge charge localization. The long lifetime in $InAlS_3$ originates from weak nonadiabatic coupling, whereas the short lifetime in Te-containing Janus layers is mainly attributed to enhanced nonadiabatic coupling between band-edge states. Our work reveals the microscopic mechanism of carrier recombination in five-atomic-layer Janus group-III chalcogenides and provides design principles for 2D

Janus materials in photovoltaic and optoelectronic applications.

Keywords: Nonadiabatic Molecular Dynamics, 2D Janus materials, Carrier Lifetime, Photocurrent

PACS: 71.15.Mb; 73.22.-f; 72.20.Jv; 72.40.+w

1. Introduction

Two-dimensional (2D) semiconductors have attracted considerable attention as promising candidates for next-generation optoelectronic, photovoltaic, and photocatalytic devices because of their atomic thickness, tunable electronic structures, strong light-matter interaction, and large specific surface area[1-10]. In these applications, the performance is not determined only by the static band structure, but also by the excited-carrier dynamics after photoexcitation[11-15]. Efficient charge separation and long carrier lifetime are highly desirable for photovoltaic and photocatalytic energy conversion[16-18], whereas fast and controllable recombination is important for light-emitting and high-speed photodetection device[19,20]. Therefore, understanding and regulating the microscopic processes of carrier relaxation, transfer, and electron-hole recombination are central issues in the design of high-performance 2D semiconductors.

Recent theoretical and experimental studies have shown that carrier dynamics can be effectively tuned by modifying electron-phonon coupling, nonadiabatic coupling, electronic decoherence, and interfacial electrostatic field[21]. For example, external electric fields can enhance interlayer charge separation in 2D van der Waals heterostructures by changing band alignment, charge redistribution[22], and electron-phonon coupling. Defect engineering can also accelerate hot-carrier relaxation by introducing intermediate electronic states and strengthening electron-phonon interaction[23]. In addition, nonadiabatic molecular dynamics (NAMD) simulations have revealed that a smaller nonadiabatic coupling between band-edge states, together with faster electronic decoherence, can suppress nonradiative electron-hole recombination and thus prolong carrier lifetime[24,25]. These

results indicate that the carrier lifetime is governed by a subtle interplay among electronic structure, lattice vibration, and charge localization, rather than by the band gap alone[26].

Among various strategies for carrier-dynamics engineering, introducing an internal electric field is particularly attractive because it can drive photogenerated electrons and holes in opposite directions without relying on external bias. Type-II van der Waals heterostructures are widely used for this purpose, since their staggered band alignment spatially separates electrons and holes and suppresses recombination[27]. However, constructing heterostructures usually requires careful lattice matching, interfacial control, and material selection. In contrast, 2D Janus materials provide an intrinsic and structurally simpler platform for generating built-in electric fields[28,29]. Owing to the different atomic species on the two surfaces, Janus structures break the out-of-plane mirror symmetry and possess permanent dipole moments perpendicular to the layer plane[30,31]. Such intrinsic dipoles can shift electrostatic potentials, redistribute band-edge charge densities, and regulate carrier separation and recombination. Recent studies on Janus transition-metal dichalcogenides monolayers have demonstrated that the built-in electric field can promote charge separation, reduce nonradiative recombination, and improve photocatalytic or photovoltaic performance[32].

Despite these advances, most previous studies have focused on Janus transition-metal dichalcogenides, Janus-based heterostructures, or electric-field-modulated van der Waals systems[33–35]. Much less attention has been paid to five-atomic-layer Janus group-III chalcogenide monolayers, although group-III chalcogenides offer rich chemical flexibility and potentially favorable optoelectronic properties[36–38]. In such systems, replacing the terminal chalcogen atoms can simultaneously tune the lattice structure, electrostatic potential difference, band gap, frontier-orbital distribution, and electron-phonon interaction[39–42]. These coupled changes may lead to a wide range of carrier recombination behaviors. However, the microscopic relationship among Janus asymmetry, band-edge

localization, nonadiabatic coupling, decoherence, and carrier lifetime remains unclear[43,44].

Motivated by these issues, we focus on five-atomic-layer Janus group-III chalcogenide monolayers as a chemically tunable platform for carrier-lifetime engineering. Using first-principles calculations combined with time-domain nonadiabatic molecular dynamics, we construct a series of MNS_3, $MNSSe_2$, and $MNSTe_2$ monolayers, where M and N represent In, Ga, and Al, and examine their structural stability, electronic properties, excited-carrier recombination, and photovoltaic response. Particular attention is paid to how the choice of group-III elements and terminal chalcogen atoms modifies the intrinsic polarity, band-edge charge distribution, nonadiabatic coupling, and electron-hole recombination pathway. By establishing the connection between Janus structural asymmetry and carrier dynamics, this work aims to provide a microscopic understanding of recombination control in five-atomic-layer Janus semiconductors and to identify useful design principles for 2D photovoltaic and optoelectronic materials.

2. Computational structures and methods

First-principles calculations were performed within density functional theory[45,46] using the Vienna Ab initio Simulation Package (VASP)[47,48]. The electron-ion interactions were described by the projector-augmented wave (PAW) method[49,50]. The exchange-correlation interaction was treated within the generalized gradient approximation using the Perdew-Burke-Ernzerhof (PBE) functional[51]. The kinetic energy cutoff for the plane-wave basis was set to 450 eV. To avoid artificial interactions between neighboring periodic images, a vacuum layer of 20 Å was inserted along the out-of-plane direction. The Brillouin zone was sampled using a 21 × 21 × 1 Monkhorst-Pack k-point grid for the primitive cells[52]. The convergence criterion for the total energy was set to 10^{-6} eV, and all atomic structures were fully relaxed until the residual force on each atom was less than 0.01 eV/Å. The Grimme DFT-D3 method was adopted to describe the weak van der Waals interaction[53].

Post-processing analyses were carried out using the VASPKIT code[54].

To evaluate the photovoltaic response of the selected monolayers, quantum transport simulations were performed using DFT combined with the nonequilibrium Green's function (NEGF) formalism[55–57], as implemented in the Nanodcal package[58]. The carrier recombination dynamics were studied by time-domain nonadiabatic molecular dynamics simulations based on time-dependent density functional theory[59] and surface-hopping dynamics(Note S1)[60,61], as implemented in the Hefei-NAMD package. Orthogonal 3 × 3 supercells containing 90 atoms were constructed for the NAMD simulations. The systems were first equilibrated at 300 K for 1 ps in the canonical ensemble. Then, ab initio molecular dynamics trajectories were generated in the microcanonical ensemble for 5 ps with a time step of 1 fs. From these trajectories, 2000 configurations were extracted for self-consistent electronic-structure calculations and nonadiabatic coupling evaluations[62].

3. Results and discussion

3.1 Structural and electronic properties

Fig. 1 shows the atomic structures of the five-atomic-layer Janus group-III chalcogenide monolayers investigated in this work. These materials can be regarded as layered structures formed by the alternating arrangement of group-III metal atomic layers and chalcogen atomic layers along the out-of-plane direction. Their general chemical formulas are MNS_3, $MNSSe_2$, and $MNSTe_2$, where M and N are selected from In, Ga, and Al. In the constructed structures, the atomic radius of M is larger than that of N (Figs 1(a), 1(b) and 1(c)). Therefore, the inequivalent arrangement of two group-III elements along the vertical direction further enhances the structural asymmetry. Meanwhile, the different chalcogen species or local chemical environments on the two surfaces break the out-of-plane mirror symmetry, giving rise to an intrinsic polarity perpendicular to the layer plane.

Such Janus structural asymmetry introduces a built-in electric field into the monolayers, which may further affect their band structures, band-edge charge

distributions, and photogenerated carrier recombination behaviors. For a fixed cation combination, the optimized lattice constant gradually increases when the terminal chalcogen atoms are changed from S to Se and Te. This trend is consistent with the increasing atomic radii of S, Se, and Te, indicating that the size effect of terminal chalcogen atoms has an important influence on the lattice structure. Therefore, the structural parameters and out-of-plane polarity of five-atomic-layer Janus group-III chalcogenides can be effectively tuned by changing the group-III element combination and terminal chalcogen species.

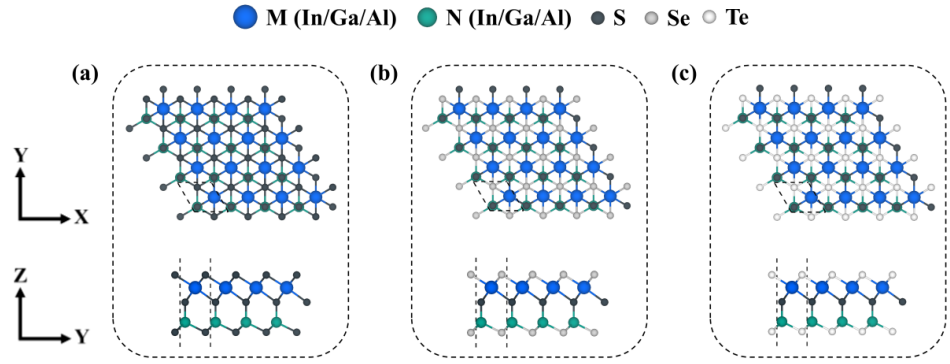


Fig. 1. Schematic diagram of the structure of five-atomic-layer Janus group-III chalcogenides (the radius of the M atom is larger than that of the N atom). (a) MNS_3, (b) $MNSSe_2$, (c) $MNSSe_2$

All nine monolayers exhibit semiconducting behavior, indicating that these five-atomic-layer Janus group-III chalcogenides have the basic electronic characteristics required for optoelectronic functional materials (Fig. S1). Among them, $GaAlS_3$, $GaAlSSe_2$, $GaAlSTe_2$, and $InAlSTe_2$ are indirect-gap semiconductors, while the other five monolayers show direct band gaps. The direct-gap feature is generally favorable for light absorption and photogenerated carrier generation, suggesting the potential advantages of these materials in optoelectronic devices.

As shown in Table 1, the band gap generally decreases with increasing lattice constant. This trend is mainly associated with the increased bond length and modified orbital hybridization induced by larger atomic sizes. For example, in the InAl-based series, the band gap decreases from 1.61 eV for $InAlS_3$ to 1.12 eV for $InAlSSe_2$ and

further to 0.69 eV for $InAlSTe_2$ (Figs S1(d), S1(e) and S1(f)). A similar trend is observed in the InGa-based series, where the band gap decreases from 0.91 eV for $InGaS_3$ to 0.47 eV for $InGaSSe_2$ and 0.42 eV for $InGaSTe_2$ (Figs S1(g), S1(h) and S1(i)). These results indicate that replacing the terminal chalcogen atoms is an effective way to regulate the electronic structures of these systems.

It is worth noting that the band gaps of these Janus monolayers cover an energy range relevant to near-infrared and visible-light responses. For photovoltaic and optoelectronic applications, a suitable band gap is beneficial for improving solar-light absorption and photogenerated carrier generation. Therefore, by selecting different group-III element combinations and terminal chalcogen species, the band gaps of five-atomic-layer Janus group-III chalcogenides can be tuned over a relatively wide range, providing possibilities for screening 2D Janus semiconductors with promising photovoltaic performance.

Table 1. Lattice constants, effective thickness (d), band gaps-PBE (E_g-PBE), band gaps-hse06 (E_g-hse06), potential differences (△V) and average built-in field (E_{eff}) of nine five-atomic-layer Janus group-III chalcogenides.

Materials	Lattice constant (Å)	d (Å)	E_g-PBE(eV)	E_g-hse06(eV)	△V (eV)	E_{eff} (V/ Å)
$GaAlS_3$	3.58	5.91	1.72	2.12	1.75	0.29
$GaAlSSe_2$	3.73	6.15	1.31	2.01	1.36	0.22
$GaAlSTe_2$	3.99	6.36	0.49	1.02	0.87	0.13
$InAlS_3$	3.74	6.09	1.61	2.48	1.93	0.31
$InAlSSe_2$	3.87	6.29	1.12	1.93	1.52	0.24
$InAlSTe_2$	4.12	6.52	0.69	1.27	1.07	0.16
$InGaS_3$	3.77	6.16	0.91	1.75	1.65	0.26
$InGaSSe_2$	3.89	6.34	0.47	1.21	1.44	0.22
$InGaSTe_2$	4.13	6.55	0.42	0.98	1.14	0.17

To further characterize the intrinsic polarity, the planar-averaged electrostatic potentials along the out-of-plane direction were calculated, as shown in Fig. 2. A distinct potential difference between the two surfaces is observed for all monolayers, confirming the presence of an intrinsic built-in electric field induced by the Janus asymmetry. The direction of the built-in electric field is from the bottom side to the top side of the monolayer. The average built-in electric field, estimated from

$E_{eff} = \frac{\triangle V}{d}$, ranges from 0.13 to 0.31 V/Å, indicating a strong internal electric field in these Janus structures. Among the investigated materials, $InAlS_3$ exhibits the largest potential difference of 1.93 eV and the strongest built-in electric field of 0.31 V/Å, whereas $GaAlSTe_2$ has the smallest potential difference of 0.87 eV and the weakest field of 0.13 V/Å. For a fixed cation pair, both the potential difference and the built-in electric field generally decrease as the terminal chalcogen atoms are changed from S to Se and then to Te. These results demonstrate that chemical substitution provides an effective means of regulating not only the band gap but also the internal electrostatic environment and built-in electric field of the Janus monolayers.

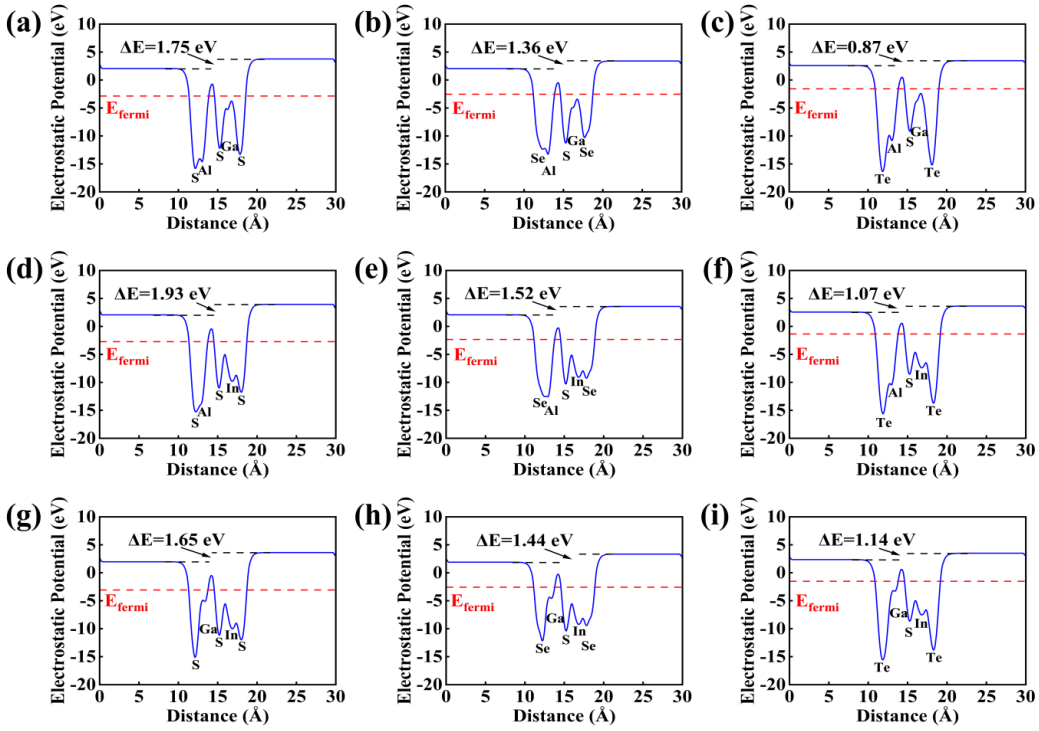


Fig. 2. Electrostatic potentials along the z-direction for monolayers (a) $GaAlS_3$, (b) $GaAlSSe_2$, (c) $GaAlSTe_2$, (d) $InAlS_3$, (e) $InAlSSe_2$, (f) $InAlSTe_2$, (g) $InGaS_3$, (h) $InGaSSe_2$, (i) $InGaSTe_2$.

The band-edge charge densities provide further insight into the possible carrier recombination behavior (Figs. S2-S4). For the GaAl-based series, $GaAlSTe_2$ exhibits the strongest localization of both VBM and CBM charge densities, indicating a relatively weak spatial separation between photogenerated holes and electrons (Fig. S2). In contrast, the InAl-based series shows a more distinct trend. The VBM charge

density of $InAlS_3$ is mainly distributed around the upper S atoms, while its CBM charge density is mainly distributed around the lower S and Al atoms, giving rise to a clear spatial separation of electrons and holes. $InAlSSe_2$ shows a similar but slightly more localized charge distribution (Fig. S3). For $InAlSTe_2$, the band-edge states become much more localized, which is expected to accelerate electron-hole recombination. The InGa-based series follows a similar tendency: $InGaS_3$ shows the most favorable spatial separation, InGaSSe2 is intermediate, and $InGaSTe_2$ exhibits the strongest localization (Fig. S4). These results suggest that the carrier lifetime should decrease in the order S-based > Se-based > Te-based monolayers for the same cation combination.

3.2 Finite-Temperature Structural Stability

As shown in Fig. 3, the thermal stability of the nine Janus monolayers was evaluated by ab initio molecular dynamics simulations at 300 K. During the simulations, most structures retained their original lattice frameworks, indicating good thermal stability at room temperature. However, $GaAlSSe_2$ and $GaAlSTe_2$ underwent obvious structural transformations, suggesting that these two monolayers are thermodynamically unstable under the present simulation conditions (Figs. 3(b) and 3(c)). Therefore, they were excluded from the following carrier-dynamics calculations.

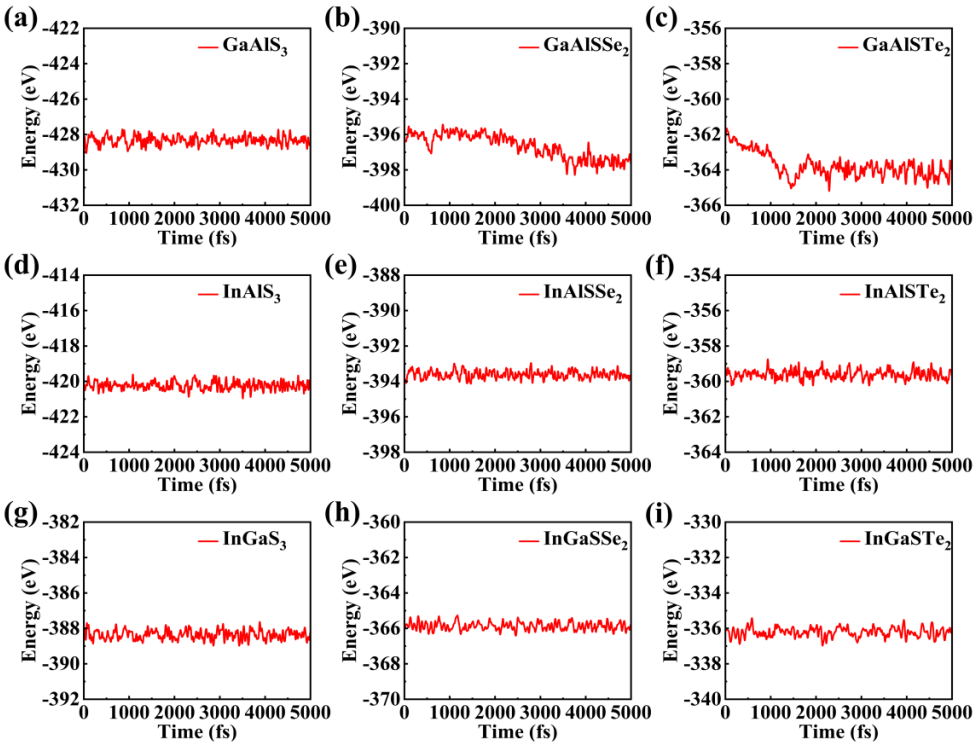


Fig. 3. Total-energy evolution during the 300 K AIMD simulations of the nine five-atomic-layer Janus group-III chalcogenide monolayers, used to examine their finite-temperature structural evolution: (a) $GaAlS_3$, (b) $GaAlSSe_2$, (c) $GaAlSTe_2$, (d) $InAlS_3$, (e) $InAlSSe_2$, (f) $InAlSTe_2$, (g) $InGaS_3$, (h) $InGaSSe_2$, (i) $InGaSTe_2$.

Although $GaAlS_3$ does not show obvious structural collapse in the AIMD simulation, it is also not included in the NAMD calculations. This is because the conduction-band minimum of $GaAlS_3$ cannot be folded to the Γ point in the orthogonal 3 × 3 supercell used for the carrier-dynamics simulations. Since the NAMD calculations require a consistent description of the band-edge states in the selected supercell, $GaAlS_3$ is excluded from the final recombination analysis. After this screening, six stable and computationally suitable monolayers remain: $InAlS_3$, $InAlSSe_2$, $InAlSTe_2$, $InGaS_3$, $InGaSSe_2$, and $InGaSTe_2$.

3.3 Carrier recombination dynamics

The electron-hole recombination dynamics of the six selected monolayers are studied using time-domain nonadiabatic molecular dynamics simulations. The time-dependent excited-state population is fitted by an exponential decay function

$f(t) = \exp(-t/\tau)$ to extract the recombination lifetime[63]. As shown in Fig. 4, the carrier lifetime can be tuned over nearly four orders of magnitude by changing the cation combination and terminal chalcogen species.

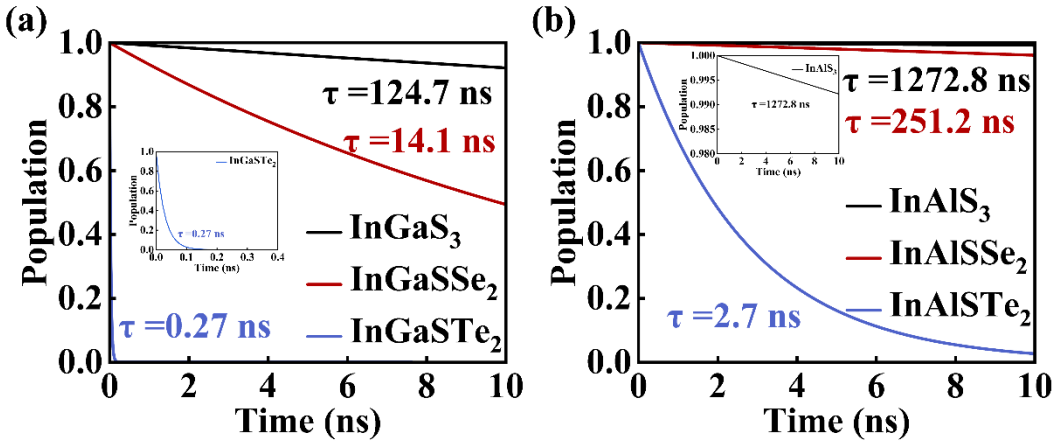


Fig. 4. (a) Time evolution of the population of the electron-hole recombination process at the CBM in $InAlS_3$, $InAlSSe_2$ and $InAlSTe_2$; (b) time evolution of the population of the electron-hole recombination process at the CBM in $InGaS_3$, $InGaSSe_2$ and $InGaSTe_2$.

For the InAl-based series, $InAlS_3$ exhibits the longest carrier lifetime of 1272.8 ns. When the terminal chalcogen atoms are changed from S to Se, the lifetime decreases to 251.2 ns for $InAlSSe_2$. A further substitution by Te dramatically shortens the lifetime to 2.7 ns for $InAlSTe_2$ (Fig. 4(a)). The same tendency is observed in the InGa-based series. The carrier lifetimes of $InGaS_3$, $InGaSSe_2$, and $InGaSTe_2$ are 124.7 ns, 14.1 ns, and 0.27 ns, respectively (Fig. 4(b)). These results clearly show that S-based Janus monolayers possess much longer carrier lifetimes than their Se- and Te-containing counterparts. Among all studied systems, $InAlS_3$ is the most promising candidate for photovoltaic applications because of its long carrier lifetime, while $InGaSTe_2$ shows the fastest electron-hole recombination.

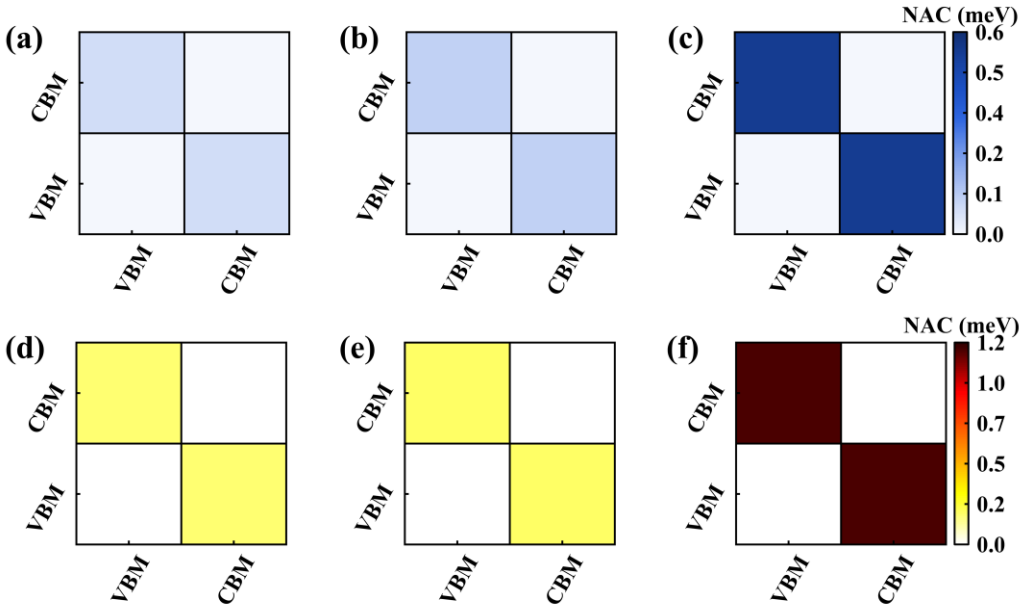


Fig. 5. Average nonadiabatic coupling (NAC) strength for electrons (holes) between donor and acceptor states along the 2000 fs NAMD trajectory at 300 K for (a) $InAlS_3$, (b) $InAlSSe_2$, (c) $InAlSTe_2$, (d) $InGaS_3$, (e) $InGaSSe_2$, (f) $InGaSTe_2$.

To understand the microscopic origin of the lifetime variation, the nonadiabatic coupling between the band-edge states is analyzed along the molecular dynamics trajectories. Its mathematical formulation can be written as[64-68]:

$$d_{jk} = \left\langle \varphi_j \middle| \frac{\partial}{\partial t} \middle| \varphi_k \right\rangle = \frac{\langle \varphi_j | \nabla_R H | \varphi_k \rangle}{\varepsilon_j - \varepsilon_k} \dot{R}, \qquad (1)$$

where H is the Kohn–Sham Hamiltonian, φ_j, φ_k, ε_j and ε_k are the wave functions and eigenvalues for electronic states j and k, and $\dot{R}$ is the velocity of the nuclei. A large NAC can effectively increases the probability of nonradiative electron-hole recombination. For the InAl-based series, the average NAC increases from $InAlS_3$ to $InAlSSe_2$ and $InAlSTe_2$, consistent with the shortening of the carrier lifetime. This indicates that the slow recombination in $InAlS_3$ originates from weak coupling between the VBM and CBM states. By contrast, the enhanced NAC in $InAlSTe_2$ provides an efficient nonradiative recombination channel, leading to a much shorter lifetime.

A similar mechanism governs the InGa-based series. $InGaSTe_2$ exhibits the strongest band-edge charge localization and the largest effective nonadiabatic

coupling, resulting in the shortest lifetime of 0.27 ns. Although the pure-dephasing time also influences the recombination process, its role is secondary compared with the NAC strength in this system. For example, $InGaSSe_2$ shows a relatively long dephasing time, but its recombination lifetime is still longer than that of $InGaSTe_2$ because the NAC strength remains the dominant factor. Therefore, the carrier recombination in these five-atomic-layer Janus group-III chalcogenides is mainly controlled by the nonadiabatic coupling associated with band-edge charge localization.

According to Eq. (1), the NAC strength is not only related to the energy separation between the initial and final states, but also depends on the electron-phonon coupling term $\langle \varphi_j | \nabla_R H | \varphi_k \rangle$ and the nuclear velocity $\dot{R}$, both of which can be characterized by phonon modes. Fig. S5 presents the phonon modes involved in the electron-hole recombination dynamics, which are obtained from the Fourier transform of the band-gap fluctuations between the VBM and CBM states. For the InAl-based series (Fig. S5(a)), the dominant phonon signals of $InAlS_3$ and $InAlSSe_2$ mainly appear in the low-frequency region (176.2 and 212.7 cm^{-1}), indicating relatively weak phonon-assisted modulation of the band-edge energy gap. In contrast, $InAlSTe_2$ shows stronger spectral features, especially in the high-frequency region (581.2 cm^{-1}), suggesting that Te substitution activates stronger lattice vibrations coupled to the band-edge states. A similar behavior is observed in the InGa-based series (Fig. S5(b)). The spectral intensity becomes more pronounced from $InGaS_3$ to $InGaSSe_2$ and $InGaSTe_2$, implying enhanced electron-phonon coupling during the recombination process. Compared with S-based monolayers, the Se- and Te-containing systems involve stronger phonon-induced band-gap fluctuations, which can increase the NAC between the VBM and CBM states and accelerate nonradiative electron-hole recombination. Therefore, the shorter carrier lifetimes in Te-containing Janus monolayers originate from stronger phonon-assisted electronic coupling, while the long lifetime of $InAlS_3$ is associated with weaker

band-edge modulation and smaller NAC. The time correlation of these band-gap fluctuations was then examined using the unnormalized autocorrelation function, $c_{jk}(t'') = [\delta E_{jk}(t')\delta E_{jk}(t-t')]_{t'}$,[69] As shown in Fig. S6, the autocorrelation functions describe how rapidly the band-gap fluctuation loses memory along the molecular dynamics trajectory. The initial value of $c_{jk}(t'')$ is related to the variance of the band-gap fluctuation and can be regarded as a measure of elastic electron-phonon scattering strength. A larger initial value usually indicates stronger fluctuation of the band-edge energy gap, while a faster decay of the autocorrelation function implies a faster loss of electronic phase memory. Therefore, the ACF analysis links the phonon-induced band-gap fluctuation to the decoherence behavior of the electronic states. Based on the second-order cumulant approximation, the pure-dephasing function can be obtained from the autocorrelation function as[70,71]

$$D(t) = \exp\left[-\frac{1}{\hbar^2}\int_0^t d\tau \int_0^\tau d\tau' C_{\mathrm{jk}}(\tau')\right]. \qquad (2)$$

The corresponding pure-dephasing functions and fitted dephasing times are shown in Fig. S7. By fitting $D(t)$ with the Gaussian form $f(t) = \exp[-t^2/2\tau^2]$, the pure-dephasing times are obtained as 2.17, 5.74, and 9.16 fs for $InAlS_3$, $InAlSSe_2$, and $InAlSTe_2$, respectively (Fig. S7(a))[72], and 10.34, 11.19, and 9.27 fs for $InGaS_3$, $InGaSSe_2$, and $InGaSTe_2$, respectively (Fig. S7(b)). These results indicate that electronic coherence is lost within several to tens of femtoseconds in these Janus monolayers. Although decoherence can influence nonradiative recombination by disturbing the coherent evolution between the VBM and CBM states, the overall lifetime trend is not governed by the dephasing time alone. For example, $InAlS_3$ has the shortest pure-dephasing time but the longest carrier lifetime, whereas $InGaSTe_2$ exhibits the fastest recombination mainly because of its strong NAC in Table S1.

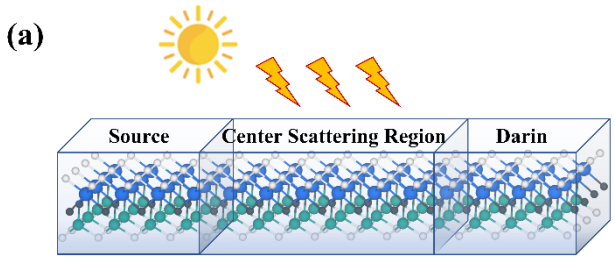
It should be noted that the PBE functional generally underestimates the band gaps of semiconductors. Therefore, the absolute recombination lifetimes may exhibit some functional dependence. However, the HSE06 calculations confirm that the band-edge orbital characters and spatial charge-separation features are qualitatively

preserved. The PBE-based NAMD results are therefore mainly used to compare the relative recombination dynamics among different Janus monolayers.

Combining the electronic-structure, charge-density, and NAMD results, a clear physical picture can be established. The intrinsic Janus polarity creates a built-in electric field and modulates the spatial distribution of band-edge states. When the VBM and CBM are spatially separated, as in $InAlS_3$, the electron-hole wave-function overlap and nonadiabatic coupling are weak, resulting in slow recombination and long carrier lifetime. When the band-edge states become more localized in the same spatial region, as in Te-containing monolayers, the electron-hole coupling is enhanced and the recombination is accelerated. These results demonstrate that intrinsic-dipole-regulated band-edge localization provides an effective route for engineering carrier lifetimes in 2D Janus group-III chalcogenides.

3.4 Photocurrent calculation

Fig 6(a) shows the schematic illustration of the photovoltaic device model based on five-atomic-layer Janus group-III chalcogenide monolayers. The device consists of a source electrode, a central scattering region, and a drain electrode[73]. Linearly polarized light is vertically incident on the monolayer, and the photocurrent response is calculated as a function of photon energy. Two polarization directions, $\theta = 0°$ and $\theta = 90°$, are considered to examine the polarization-dependent photovoltaic response[74]. Owing to the intrinsic out-of-plane polarity and the built-in electric field discussed above, these Janus monolayers are expected to promote the separation of photogenerated electrons and holes, which is beneficial for photocurrent generation[75].



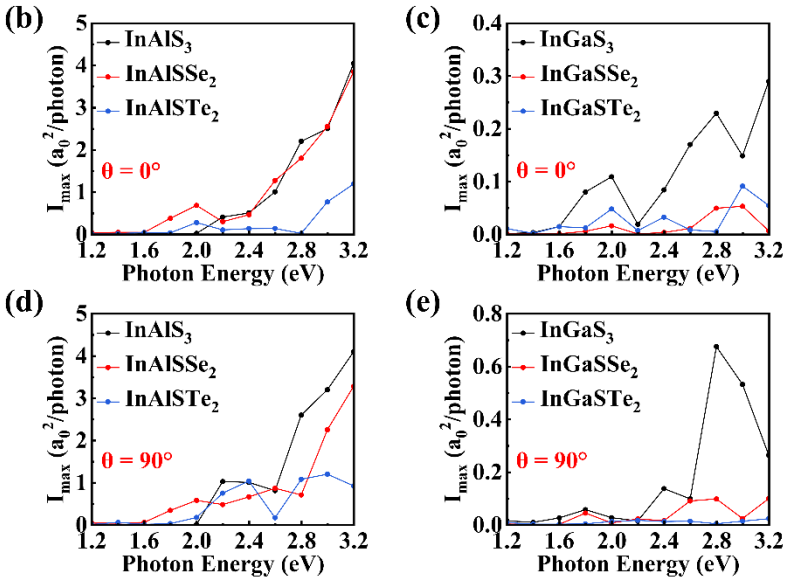


Fig. 6. (a) Schematic illustration of the photovoltaic device based on five-atomic-layer Janus group-III chalcogenide monolayers. Photocurrent spectra under linearly polarized light illumination for (b) $InAlS_3$, $InAlSSe_2$, and $InAlSTe_2$ at θ = 0°, (c) $InGaS_3$, $InGaSSe_2$, and $InGaSTe_2$ at θ = 0°, (d) $InAlS_3$, $InAlSSe_2$, and $InAlSTe_2$ at θ = 90°, and (e) $InGaS_3$, $InGaSSe_2$, and $InGaSTe_2$ at θ = 90°.

Figs 6(b) and 6(d) show the photocurrent spectra of the InAl-based monolayers under linearly polarized light with θ = 0° and θ = 90°, respectively. The photocurrent generally increases with increasing photon energy, indicating that higher-energy photons can excite more effective electronic transitions and contribute to charge transport. Among the three InAl-based monolayers, $InAlS_3$ exhibits the strongest photocurrent response, with a maximum value of 4.13 a_0^2/photon. $InAlSSe_2$ also shows a pronounced photoresponse, whereas $InAlSTe_2$ gives a much weaker photocurrent. This trend is consistent with the carrier recombination dynamics discussed above. The long carrier lifetime and weak nonadiabatic coupling in $InAlS_3$ allow photogenerated carriers to survive for a longer time, thereby improving their probability of being extracted by the electrodes. In contrast, the faster recombination in $InAlSTe_2$ suppresses effective carrier collection and leads to a lower photocurrent response.

The InGa-based monolayers show a similar but much weaker photovoltaic

response, as shown in Figs. 6(c) and 6(e). Compared with the InAl-based systems, the photocurrents of $InGaS_3$, $InGaSSe_2$, and $InGaSTe_2$ are significantly smaller. This difference can also be understood from their recombination behavior. The InGa-based monolayers generally possess shorter carrier lifetimes and stronger nonadiabatic coupling than the corresponding InAl-based monolayers, which increases the probability of electron-hole recombination before carrier extraction. In particular, $InGaSTe_2$ shows the shortest recombination lifetime and therefore exhibits an unfavorable photovoltaic response. These results indicate that suppressing nonradiative recombination is essential for enhancing the photocurrent of five-atomic-layer Janus group-III chalcogenides.

The polarization dependence of the photocurrent further reflects the anisotropic optical response of these monolayers. For both InAl- and InGa-based systems, the photocurrent spectra at $\theta = 0°$ and $\theta = 90°$ show different intensities, suggesting that the photoexcited carrier transport is sensitive to the direction of light polarization. Such anisotropic photocurrent behavior may originate from the anisotropic orbital distribution near the band edges and the direction-dependent transition probability under linearly polarized light. Therefore, in addition to chemical substitution, light polarization provides another possible degree of freedom for modulating the photovoltaic response of these Janus monolayers.

To further evaluate the photovoltaic potential of these Janus monolayers, their optical absorption spectra were also calculated, as shown in Fig. S8. $InAlS_3$ exhibits appreciable optical absorption in the energy range of 2.0–3.2 eV, which partially overlaps with the visible region of the solar spectrum. Although its absorption strength is not the highest among the investigated monolayers, the observed optical response indicates that $InAlS_3$ can effectively utilize part of the visible-light region. Therefore, the photovoltaic potential of $InAlS_3$ should be attributed to the combined contribution of its suitable band gap, effective carrier transport, relatively long carrier lifetime, strong photocurrent response, and appreciable optical absorption, rather than to superior performance in a single property.

The underestimated PBE band gaps may shift the calculated absorption edge and photocurrent onset toward lower photon energies. Consequently, the absolute photocurrent values and the low-energy onset should be interpreted with caution. Nevertheless, the relative photocurrent response among the investigated systems and the associated influence of the built-in electric field remain meaningful at the present level of theory.

Overall, the photocurrent calculations confirm the photovoltaic potential of the screened five-atomic-layer Janus group-III chalcogenides. $InAlS_3$ combines a suitable band gap, strong intrinsic polarity, clear band-edge charge separation, weak NAC, long carrier lifetime, and the largest photocurrent response among the investigated systems. These advantages make $InAlS_3$ the most promising candidate for high-efficiency photovoltaic applications in this material family.

3. Conclusion

Although the exact Janus monolayers studied here have not yet been experimentally reported, they may be synthesized by combining thin-film growth with selective surface-chalcogen exchange. S-rich systems, particularly $InAlS_3$, are expected to be more experimentally accessible because of their relatively high chemical stability. $InAlS_3$ is a promising target for future experiments owing to its suitable band gap, strong intrinsic polarity, clear band-edge charge separation, weak nonadiabatic coupling, and long carrier lifetime. Its structural, optical, and photovoltaic properties could be examined using electron microscopy, Raman spectroscopy, time-resolved photoluminescence, transient absorption, and photocurrent measurements. Thus, this work provides experimentally testable predictions for future Janus photovoltaic materials.

In summary, we systematically investigated five-atomic-layer Janus group-III chalcogenide monolayers using first-principles calculations, NAMD simulations, and NEGF transport calculations. The intrinsic Janus polarity induces built-in electric fields and regulates the spatial distribution of band-edge states, thereby strongly

affecting carrier recombination. After stability screening, six monolayers were selected for carrier-dynamics calculations. Their recombination lifetimes vary from 0.27 ns in $InGaSTe_2$ to 1272.8 ns in $InAlS_3$, showing a change over more than four orders of magnitude. This large lifetime variation is mainly governed by the nonadiabatic coupling associated with band-edge charge localization, rather than by the band gap or pure-dephasing time alone. $InAlS_3$ exhibits spatially separated VBM and CBM states, weak nonadiabatic coupling, long carrier lifetime, and the strongest photocurrent response of 4.13 a_0^2/photon. These results identify $InAlS_3$ as a promising 2D photovoltaic candidate and suggest that intrinsic-dipole engineering is an effective strategy for regulating carrier lifetime and photoresponse in Janus semiconductors.

ACKNOWLEDGEMENTS

This work is supported by the National Natural Science Foundation of China (Grant Nos. 12304220, 12174157, 12074150, 12404051), the Natural Science Foundation of Jiangsu Province (Nos. BK20230518, BK20230516), the China Postdoctoral Science Foundation (No. 2023M731383).

References

[1] Novoselov K S, Jiang D, Schedin F, Booth T J, Khotkevich V V, Morozov S V and Geim A K 2005 Proc. Natl. Acad. Sci. U. S. A. 102 10451

[2] Butler S Z, Hollen S M, Cao L, Cui Y, Gupta J A, Gutiérrez H R, Heinz T F, Hong S S, Huang J, Ismach A F, Johnston-Halperin E, Kuno M, Plashnitsa V V, Robinson R D, Ruoff R S, Salahuddin S, Shan J, Shi L, Spencer M G, Terrones M, Windl W and Goldberger J E 2013 ACS Nano 7 2898

[3] Chen S, Gao J F, Srinivasan B M, Zhang G, Yang M, Cha J W, Wang S J, Chi D Z and Zhang Y W 2019 ACS Appl. Mater. Interfaces 11 46090

[4] Mak K F, Lee C, Hone J, Shan J and Heinz T F 2010 Phys. Rev. Lett. 105 136805

[5] Splendiani A, Sun L, Zhang Y, Li T, Kim J, Chim C Y, Galli G and Wang F 2010

Nano Lett. 10 1271

[6] Xia F, Wang H, Xiao D, Dubey M and Ramasubramaniam A 2014 Nat. Photonics 8 899

[7] Song Y R, Ren Y H, Cheng H J, Jiao Y Y, Shi S B, Gao L H, Xie H M, Gao J F, Sun L C and Hou J A 2023 Angew. Chem. Int. Ed. 62 e202306420

[8] Mak K F and Shan J 2016 Nat. Photonics 10 216

[9] Zhao Y, Zhang S, Shi R, Waterhouse G I N, Tang J and Zhang T 2020 Mater. Today 34 78

[10] Liu X J, Gao J F, Zhang G and Zhang Y W 2018 Nanoscale 10 19854

[11] Buscema M, Island J O, Groenendijk D J, Blanter S I, Steele G A, van der Zant H S J and Castellanos-Gomez A 2015 Chem. Soc. Rev. 44 3691

[12] Kozawa D, Kumar R, Carvalho A, Kumar A K, Zhao W, Wang S, Toh M, Ribeiro R M, Castro Neto A H, Matsuda K and Eda G 2014 Nat. Commun. 5 4543

[13] Wang Y, Kim J C, Wu R J, Martinez J, Song X, Yang J, Zhao F, Mkhoyan K A, Jeong H Y and Chhowalla M 2019 Nature 568 70

[14] Hong X, Kim J, Shi S F, Zhang Y, Jin C, Sun Y, Tongay S, Wu J, Zhang Y and Wang F 2014 Nat. Nanotechnol. 9 682

[15] Li Q, Wu J B, Huang L, Gao J F, Zhou H W, Shi Y J, Pan Q H, Zhang G, Du Y and Liang W X 2018 J. Mater. Chem. A 6 12115

[16] Bernardi M, Palummo M and Grossman J C 2013 Nano Lett. 13 3664

[17] Tsai M L, Su S H, Chang J K, Tsai D S, Chen C H, Wu C I, Li L J, Chen L J and He J H 2014 ACS Nano 8 8317

[18] Gao J F, Cheng Y, Tian T, Hu X L, Zeng K Y, Zhang G and Zhang Y W 2017 ACS Omega 2 8640

[19] Pospischil A, Furchi M M and Mueller T 2014 Nat. Nanotechnol. 9 257

[20] Wang H, Zhang C, Chan W, Manolatou C, Tiwari S and Rana F 2016 Phys. Rev. B 93 045407

[21] Zheng Q, Saidi W A, Xie Y, Lan Z, Prezhdo O V, Petek H and Zhao J 2017 Nano Lett. 17 6435.

[22] Chaves A, Azadani J G, Ozcelik V O, Grassi R and Low T 2018 Phys. Rev. B 98 121302

[23] Wu Y, Chu W, Vasenko A S and Prezhdo O V 2021 J. Phys. Chem. Lett. 12 8699.

[24] Song B, Liu L and Yam C 2019 J. Phys. Chem. Lett. 10 5564

[25] Fu C F, Zheng Q J, Li X X and Yang J L 2024 Nano Lett. 24 6425

[26] Zheng Q, Xie Y, Lan Z, Prezhdo O V, Saidi W A and Zhao J 2018 Phys. Rev. B 97 205417

[27] Kang J, Tongay S, Zhou J, Li J and Wu J 2013 Appl. Phys. Lett. 102 012111

[28] Riis-Jensen A C, Pandey M and Thygesen K S 2018 J. Phys. Chem. C 122 24520

[29] Fu L, Li S, Bo X, Ma S, Li F and Pu Y 2024 Chin. Phys. B 33 096301

[30] Bian C, Shi J, Liu X, Yang Y, Yang H and Gao H 2022 Chin. Phys. B 31 097304

[31] Qi Y, Zhao J and Zeng H 2024 Chin. Phys. B 33 096302

[32] Qi Y, Zhao J and Zeng H 2024 Chin. Phys. B 33 096302

[33] Cai H, Gu Y, Lin Y C, Yu Y, Geohegan D B and Xiao K 2019 Appl. Phys. Rev. 6 041312

[34] Ma Z, Zhou T, Duan W and Huang Y 2023 J. Mater. Chem. C 11 16439

[35] Demirci S, Avazlı N, Durgun E and Cahangirov S 2017 Phys. Rev. B 95 115409

[36] Zhuang H L and Hennig R G 2013 Chem. Mater. 25 3232

[37] Guo Y, Zhou S, Bai Y and Zhao J 2017 Appl. Phys. Lett. 110 163102

[38] Wan W, Zhao S, Ge Y and Liu Y 2019 J. Phys.: Condens. Matter 31 435501

[39] Vu T V and Hieu N N 2022 J. Phys.: Condens. Matter 34 115601

[40] Pang K, Wei Y, Xu X, Ying T, Li W, Li X, Yang J, Jiang Y and Tian W Q 2021 J. Phys. Chem. C 125 11285

[41] Zhao Y, Tan Q, Li H, Li Z, Wang Y and Ma L 2024 Sci. Rep. 14 10698

[42] Querne M B P, Dias A C, Janotti A, da Silva J L F and Lima M P 2024 J. Phys. Chem. C 128 12164

[43] Kumar V and Jung J 2022 Bull. Korean Chem. Soc. 43 138

[44] Tran T A, Hai L S, Vi V T T, Nguyen C Q, Nghiem N T, Thao L T P and Hieu N N 2023 RSC Adv. 13 12153

[45] Hohenberg P and Kohn W 1964 Phys. Rev. 136 B864

[46] Kohn W and Sham L J 1965 Phys. Rev. 140 A1133

[47] Kresse G and Hafner J 1993 Phys. Rev. B 47 558

[48] Kresse G and Furthmüller J 1996 Phys. Rev. B 54 11169

[49] Blöchl P E 1994 Phys. Rev. B 50 17953

[50] Kresse G and Joubert D 1999 Phys. Rev. B 59 1758

[51] Perdew J P, Burke K and Ernzerhof M 1996 Phys. Rev. Lett. 77 3865

[52] Monkhorst H J and Pack J D 1976 Phys. Rev. B 13 5188

[53] Grimme S, Antony J, Ehrlich S and Krieg H 2010 J. Chem. Phys. 132 154104

[54] Wang V, Xu N, Liu J C, Tang G and Geng W T 2021 Comput. Phys. Commun. 267 108033

[55] Taylor J, Guo H and Wang J 2001 Phys. Rev. B 63 245407

[56] Brandbyge M, Mozos J L, Ordejón P, Taylor J and Stokbro K 2002 Phys. Rev. B 65 165401

[57] Maassen J, Harb M, Michaud-Rioux V, Zhu Y and Guo H 2013 Proc. IEEE 101 518

[58] Zhang L, Gong K, Chen J, Liu L, Zhu Y, Xiao D and Guo H 2014 Phys. Rev. B 90 195428

[59] Runge E and Gross E K U 1984 Phys. Rev. Lett. 52 997

[60] Tully J C 1990 J. Chem. Phys. 93 1061

[61] Craig C F, Duncan W R and Prezhdo O V 2005 Phys. Rev. Lett. 95 163001

[62] Akimov A V and Prezhdo O V 2013 J. Chem. Theory Comput. 9 4959

[63] Wang S, Huang M, Wu Y N, Chu W, Zhao J, Walsh A, Gong X G, Wei S H and Chen S 2022 Nat. Comput. Sci. 2 486

[64] Tapavicza E, Tavernelli I and Rothlisberger U 2007 Phys. Rev. Lett. 98 023001

[65] Tavernelli I, Tapavicza E and Rothlisberger U 2009 J. Chem. Phys. 130 124107

[66] Yao L, Jiang X, Zheng Q and Zhao J 2026 Chin. Phys. Lett. 43 010701

[67] Akimov A V and Prezhdo O V 2014 J. Chem. Theory Comput. 10 789

[68] Duncan W R, Craig C F and Prezhdo O V 2007 J. Am. Chem. Soc. 129 8528

[69] Mallus M I, Aghtar M, Chandrasekaran S, Lüdemann G, Elstner M and Kleinekathöfer U 2016 J. Phys. Chem. Lett. 7 1102

[70] Sifain A E, Wang L, Tretiak S and Prezhdo O V 2019 J. Chem. Phys. 150 194104

[71] Kilina S V, Neukirch A J, Habenicht B F, Kilin D S and Prezhdo O V 2013 Phys. Rev. Lett. 110 180404

[72] Liu J, Kilina S V, Tretiak S and Prezhdo O V 2015 ACS Nano 9 9106

[73] Luo W M, Shao Z G and Yang M 2019 Nanoscale Res. Lett. 14 380

[74] Zhang L W, Yang Y Q, Chen J and Zhang L 2023 Front. Phys. 18 62301

[75] Sun N and Ye H 2023 Appl. Phys. Lett. 123 211107